Proceedings of the ASME 2010 3rd Joint US-European Fluids Engineering Summer Meeting and 8th International Conference on Nanochannels, Microchannels, and Minichannels
FEDSM-ICNMM2010
August 1-5, 2010, Montreal, Canada

FEDSM-ICNMM2010-30182

ANALYTICAL MODEL OF DIURNAL TEMPERATURE FOR A RADOME ENCLOSED ANTENNA

Anthony A. DiCarlo*

MITRE Corporation,
202 Burlington Road, Bedford, Massachusetts 01730-1420,
U.S.A.

ABSTRACT

A critical design consideration for the Haystack Ultrawide-band Satellite Imaging Radar's (HUSIR) with respect to its performance at W-band is thermal distortion. This is because thermal distortion affects the surface accuracy of a parabolic reflector. For example, an extremely tight surface tolerance, ~100 microns root-mean-squared, is required to obtain antenna performance efficiency close to 85 percent. Thermal control is one method for mitigating this distortion. Cost effective thermal control relies on a model that rapidly and accurately predicts the antenna's temperature. This work develops a simplified analytical model to predict the surface temperature of a metal antenna based on external diurnal temperature variations. The thermal energy balance of the radome/antenna captures the radome enclosed antenna temperature transients. This study also includes a parametric investigation to quantify the sensitivity of the model with respect to convection coefficients. The developed model generates results for four months, (February, April, August, and October). We compare some of these results to experimental measurements.

1 INTRODUCTION

As part of the Haystack Ultrawide-band Satellite Imaging Radar (HUSIR) project, the Air Force plans to upgrade the existing Haystack tracking and imaging radar to increase its resolution for imaging satellites. The Haystack antenna, which was designed in 1960 and is located in Massachusetts and straddles the towns of Westford, Groton and Tyngsboro, is a fully steerable, altitude-over-azimuth-Cassegrain, radome-enclosed antenna that is still in operation today and is utilized by several government organizations including the Joint Space Operations Center and the National Air and Space Intelligence Center [1]. The Air Force provided funding to Massachusetts Institute of Technology/Lincoln Laboratory (MIT/LL) to upgrade the existing Haystack antenna from X-band to both X-band and W-band. Because HUSIR is located in New England and subjected to the area's ever changing weather conditions, the impact of the four seasons plays a significant role in W-band performance.

The new radar will be capable of both X- and W-band. The W-band capability requires a smoother surface tolerance than the current Haystack antenna. The mitigation of thermal distortion is a necessity for high frequency antennas. According to the Ruze equation [2], equation 1, the surface tolerance required at W-band for an 85 % efficiency is approximately 100 um measured from the nominal parabolic surface. Where n_a is the efficiency of the surface, λ is the wavelength, and ε is the square root of the mean-squared-half-pathlength deviation of the reflecting surface from the nominal parabolic surface.

$$n_a = e^{-\left(\frac{4\pi\varepsilon}{\lambda}\right)^2} \tag{1}$$

In this design, human comfort is not of paramount importance. To develop an effective heating, ventilation and air conditioning (HVAC) system while minimizing energy costs, a designer must understand the antenna's transient temperature variations. The gradient temperature distortion due to air stratification and the changes in reference temperature were minor when compared to the diurnal changes. Considerable research has been conducted in gradient models of large enclosures, stadiums and aircraft hangers [3,4,5]. If necessary, the modeling approach may be improved by implementing these methods. Changes from a reference temperature or built temperature are not as concerning since effective compensation can be performed with regard to homologous deformation. The diurnal temperature variations are most detrimental to the antenna performance and therefore presented herein.

* Author of correspondence, Email: adicarlo@mitre.com.

Unfortunately, the availability of literature on internal thermal analysis of dome-enclosed antennas is quite limited. What is available pertains to the thermal behavior of antenna back-structure enclosed telescopes for high precision radio telescopes [6,7]. Particularly interesting among this material is the sub-reflector compensation method that utilizes temperature fields [8]. This compensation method would alleviate some of the demands on the HVAC system. The focus of the literature available differs from that of our current design challenge entailing the radome, which involves a large volume of air.

Considerably complex approaches for thermal characterization of buildings [9] can be implemented. Although use of computational fluid dynamics (CFD) may be most accurate, it would not be practical in terms of the amount of time required to implement it with a controlling algorithm. The benefit of a simple analytical model is that it offers quick computing time and stability. This is especially true when compared to CFD models where it would be impractical to implement these models in a control algorithm due to the time required to compute the field. Furthermore, Gao [10] showed good comparison between multi-layer models and CFD simulations. Multi-zone network models [11] and zonal models [12] may be also appropriate. It is also worthwhile to mention that a logical progression of this work is the adaptation of methods in airflow and thermal transport in a large dome employing a three-dimensional thermal and airflow (3D-TAF) model [13]. The analytical model applied herein uses approaches similar to greenhouse analyses [14]. The developed model represents the radome as a large, single cell building. This first-order method has relatively low computational costs and is simple to implement.

2 SEASONAL MEAN DAILY VARIATIONS

The prime contractor, MIT/LL collected the daily outdoor temperatures for 2006. The monthly mean daily temperature variations for the four months representing winter, spring, summer, and autumn were computed and plotted as a function of Greenwich Mean Time, Fig. 3.

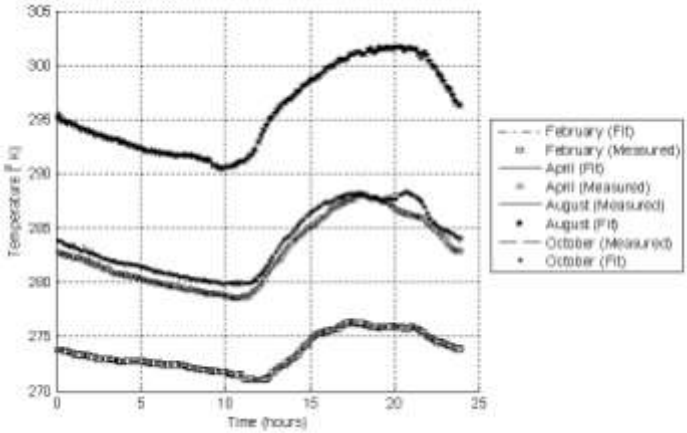

Figure 1. Monthly mean diurnal variation for 2006. Daily temperature cycles representative of four seasons.

Diurnal temperatures illustrate a periodic characteristic that lends itself to harmonic representation via Fourier series. The coldest month, February, has the least fluctuation in terms of daily temperature swings, while the warmest month, August, has the most fluctuation. There is less variation in the nighttime temperature. The correlation is that solar heat contributes notably to the daily variation.

The pattern of the Sun rising and setting drives the diurnal temperature cycle. The intensity and solar heat flux vary depending on the time of day as well as the time of year. Variations throughout the year are connected to the Earth's tilt with respect to the Sun. Fig. 2 plots the intensity attained from ASHREA standard [15].

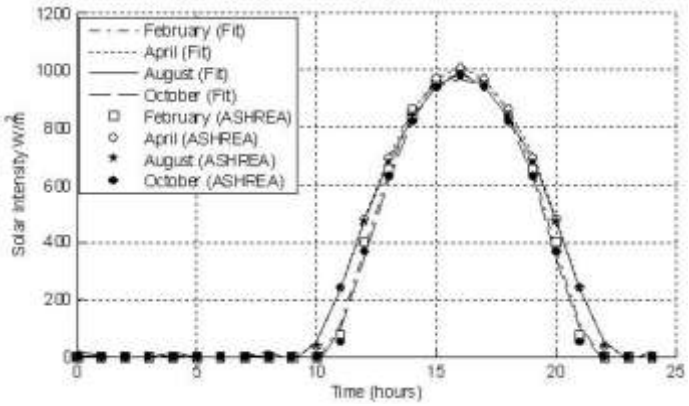

Figure 2. Daily solar intensity pattern at 40 deg North Latitude.

Due to the periodic nature of the ambient temperatures and the solar intensity, the resultant temperature in the radome is also periodic. Therefore, it is reasonable to represent the data using Fourier series with sixth-degree trigonometric polynomial approximation. Six harmonics proved adequate for this case as shown in Fig. 2 and Fig. 3 by comparison of the fitted curve from Fourier series and measured curves. The following sections will apply these approximations to acquire analytical estimations.

3 RADOME/ANTENNA SCHEMATIC AND TRANSIENT AIR ANALYTICAL MODELFINITE ELEMENT FORMULATION

This section provides an analytical model derived from fundamental heat transfer equations. In particular, the work commences with an energy balance of the external ambient air and the internal radome air as well as an energy balance of the internal air and surface temperature of the antenna structure. These two differential equations are combined to form a single second order governing equation.

The radome houses the antenna structure and protects it from the external environment, Fig. 3. In the present model, the mass of the antenna structure, m_s, and the air, m_a, are 280670 kg and 55760 kg, respectively. The specific heat of the structure, C_{ps}, and the air, C_{pa}, are evaluated at 750 and 1000 J/kg K, respectively. The surface area of the radome, A_r, and the structure, A_s, are to be 5830 and 2615 m^2, respectively.

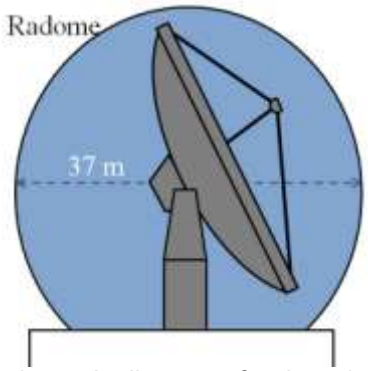

Figure 3. Schematic diagram of radome/antenna

The Sun's radiation projects onto the radome. In this study, the truncation at the bottom of the radome is not significant and therefore was not taken into account in the following equations. The projected area is simply πR^2, where R is the radome's radius. Subtraction of the projection area from the total area produces the shaded area. A white radome reflects 68% of solar incident energy [18]. Therefore, the energy absorbed by the radome's surface is equal to 32%. Not all of the absorbed energy enters the radome enclosure; some heat convects off the external surface. Based on the 1/3 ratio of external to internal convection coefficient, this analysis assumes approximately 10% of the Sun's radiation is absorbed into the radome enclosure.

A convection heat transfer equation [16] was employed to calculate the temperature of the internal air, T_a, for a given external ambient temperature, T_∞, equation 2. Thermal conduction through the radome wall is a minor impedance to the heat transfer. Therefore, it is reasonable not to include this term.

$$m_a C_{pa} \frac{dT_a}{dt} = Q_{solar} A_{proj} + h_{tot} A_r \left(T_\infty - T_a\right) \tag{2}$$

We assume the heat convection equation also governs the heat transfer to the surface of the antenna structure, T_s, from the internal air, equation 3.

$$m_s C_{ps} \frac{dT_s}{dt} = h_a A_s \left(T_a - T_s\right) \tag{3}$$

We reduce this pair of first order differential equations to a second order differential equation by solving for Ta in equation 3 and substitute back into equation (2) to get equation 4.

$$\frac{d^2 T_s}{dt^2} + 2b \frac{dT_s}{dt} + a^2 T_s = c\left(Q_{solar} A_{proj} + h_{tot} A_r T_\infty\right) \tag{4}$$

where

$$b = \frac{m_a C_{pa} A_s h_a + h_{tot} A_r m_s C_{ps}}{2\left(m_a C_{pa} m_s C_{ps}\right)}, \quad a = \sqrt{\frac{h_{tot} A_r A_s h_a}{m_a C_{pa} m_s C_{ps}}}, \quad \text{and}$$

$$c = \frac{h_a A_s}{m_a C_{pa} m_s C_{ps}}$$

Since a Fourier series can represent the solar loading and external ambient temperatures on the left hand side of equation 4, the temperature on the surface of the antenna results in a periodic solution to equation 4, equation 5.

$$T_s(t) = C_1 e^{\left(\left(-b+\sqrt{b^2-a^2}\right)t\right)} + C_2 e^{\left(\left(-b-\sqrt{b^2-a^2}\right)t\right)} + \ldots$$
$$c\left(\frac{A_o}{a^2} + \sum_1^n \begin{pmatrix} A_n \dfrac{\left(a^2-\omega_n{}^2\right)\cos(\omega_n t) + 2\omega_n b \sin(\omega_n t)}{\omega_n{}^4 + \left(4b^2-2a^2\right)\omega_n{}^2 + a^4} + \ldots \\ B_n \dfrac{\left(a^2-\omega_n{}^2\right)\sin(\omega_n t) - 2\omega_n b \cos(\omega_n t)}{\omega_n{}^4 + \left(4b^2-2a^2\right)\omega_n{}^2 + a^4} \end{pmatrix}\right) \tag{5}$$

where $\omega_n = 2\pi n / 24hr$, $A_o = Q_{solar\_o} A_{proj} + h_{tot} A_r T_{\infty\_o}$,
$A_n = Q_{solar\_An} A_{proj} + h_{tot} A_r T_{\infty\_An}$, and
$B_n = Q_{solar\_Bn} A_{proj} + h_{tot} A_r T_{\infty\_Bn}$

The constants $T_{\infty}\_A_n$, $T_{\infty}\_B_n$, $Q_{solar}\_A_n$, and $Q_{solar}\_B_n$ for equation 5 are provided in the appendix. These values for ambient temperature and solar intensity were obtained from the temperature measurements and the ASHRAE data, shown previously in Figure 1 and 2, respectively.

Coefficients for convective heat transport are typically difficult to quantify. As part of this study, we investigated the surface convection coefficient for the external radome surface when subjected to wind and solar conditions to determine the appropriate value. This investigation consisted of values calculated from analytical methods [17], values computed in a CFD model of the airflow over the radome, recommended values by the radome manufacturer [18], and values calculated from measurements. Table 1 provides a summary of these values.

	3 Mile per Hour	15 Mile per Hour
Flat Plate Calculated	7.5	27
Sphere (windward)	0.8	1.9
CFD Summer (max)	4.9	18.2
CFD Winter (max)	5.0	19.3
Analysis Free Convection	2.7	
Empirical Summer Overall	7.6	

Table. Convection Coefficient Summary, W/m^{2}K

Based on the data reviewed, it was determined that the average convection coefficients of 5 internally and 15 W/m^{2}K externally provided the most realistic description data evaluated.

4 RESULTS AND DISCUSSION

This section presents and discusses the calculated results of the developed analytical model when predicting the diurnal antenna surface temperature. The model predicts the temperature variation for the four months representative of

spring, summer, fall, and winter. The model takes into account periodic behavior as well as transient behavior.

Fig. 4 plots the mean of the actual temperature profile on the antenna structure, *Ts Measured*, estimated from August data collected at five locations on the antenna; top, bottom, left, right, and center. Error bars represent the standard deviation of this data. This deviation is an indication of the gradients in the vertical and horizontal direction. Also plotted in this figure are the external ambient temperature, T_∞, and the predicted antenna surface temperature, T_s *Predicted*. Although there appears to be close agreement between the predicted and measured values, there is some peculiarity with the responsiveness of the measured data when compared to the external temperatures. For this reason, the analytical model appears more realistic than the measure data.

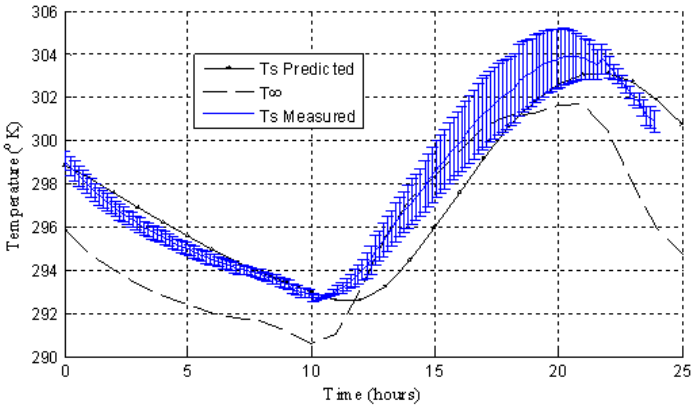

Figure 4. Comparison of measured and predicted temperatures for August, 2006.

The discrepancy, a two to three hour time lag between the measured and predicted values, was more apparent during sunrise. This indicates that the temperature sensors located on the antenna surface may require better insulation. Another hypothesis for this sensitivity is that the contribution of the solar radiation transmission through the radome, transmissivity, may be more significant than originally anticipated. The radome manufacturer estimated the radiation to be approximately 0.3% of the solar load, negligible to these estimations [18]. Notwithstanding this anomaly, the measured data still provides a degree of validation for this model.

Heat transfer coefficients are difficult to predict due to the dependence on airflow and geometry location. This study sought to explore the sensitivity of heat transfer coefficients for the radome and the antenna. The range of external values on the radome due to 3 Mile per hour, 15 Mile per hour wind, and natural convection was from 2 W/m^{2}K to 30 W/m^{2}K. Fig. 2 illustrates the model's sensitivity to the convection coefficient at the radome's surface, ho, and at the antenna's surface, ha. Fig. 5 presents the results calculated with antenna coefficients of 5 and 10 W/m^{2}K using the derived analytical model. This variation has a minor impact when taken into account for accuracy. A notable impact to the prediction occurs at low radome convection coefficients. The low coefficient of 2 W/m^{2}K is not typical and should be viewed as a rare upper bound.

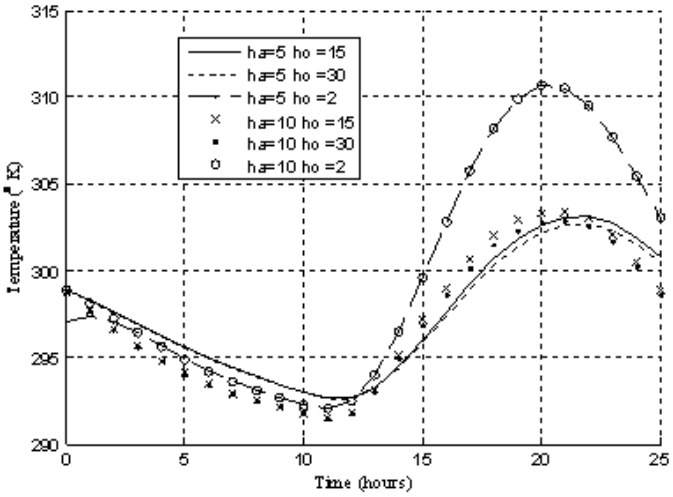

Figure 5. Sensitivity of the convection coefficients.

Fig. 6 plots the external temperatures for February, April, August, and October along with the periodic antenna surface temperatures calculated with the analytical model.

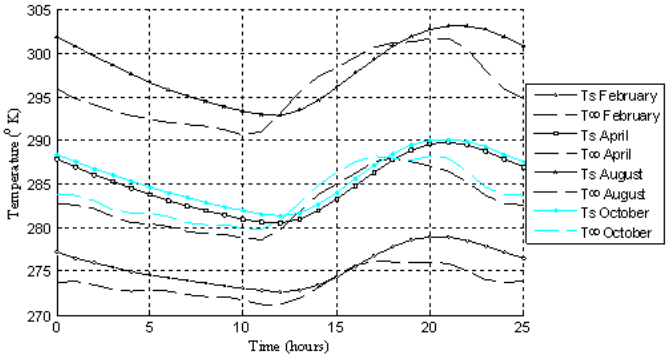

Figure 6. Predicted antenna diurnal temperature variations for February, April, August, and October are plotted along with measured external temperatures.

Fig. 6 does not include the particular contribution of the second order differential equation. The April and October data are in close agreement as expected.

Since the antenna is comprised of various sized truss members, each member reaching thermal equilibrium at a different rate based primarily on cross-sectional geometric properties. Fig. 6 illustrates that the greatest temperature variations occur during the summer months. Hence, most distortion could occur during the summer months and the least amount during the winter months.

5 CONCLUDING REMARKS

This study developed a simplified analytical model at the macroscopic flow level for predicting the temperature variations of the antenna structure. This model shows promising features in serving as a simple tool to predict the radome's internal temperatures. This represents an advantage over methods that are too computationally intensive (e.g. CFD). Hence, it can lead to cost effective design and control of a HVAC system. Diurnal temperature measurements

presented validate this model. Further work is to improve the accuracy of this model via multi-zone approximation and possibly comparison to CFD.

6 ACKNOWLEDGEMENTS

This work was motivated and supported by the HUSIR Program Office in an ongoing effort to upgrade the Haystack antenna to both X-band and W-band. I would also like to thank Dr. Keith Doyle for valuable discussions and MIT Haystack Observatory for measured data.

7 REFERENCES

[1] Rhoades, G., J. Cardiasmenos, A.G., Antebi, F. Kan, D. Valentine, A. Sarawit, M. Brenner, 2007, "The New Haystack Antenna – Structural Design, Optimization, and Performance Overview," *Proceedings of IEEE Radar Conference,* pp 156-164.

[2] Ruze, J., 1966, "Antenna Tolerance Theory-A review," *Proceedings of IEEE*, **54(**4), pp. 633-640.

[3] Nishioka, T., K. Ohtaka, N. Hashimoto, H. Onojima, 2000, "Measurement and evaluation of the indoor thermal environment in a large domed stadium," *Energy and Buildings*, **32**(2),pp 217–223.

[4] Said, M.N.A, R.A. MacDonald, G.C. Durrant, 1996, "Measurement of thermal stratification in large single-cell buildings," *Energy and Buildings* **24**(2) 105–115.

[5] Wang, X., C. Huang, W.Cao, 2009, "Mathematical modeling and experimental study on vertical temperature distribution of hybrid ventilation in an atrium building," *Energy and Buildings*, **41**(9), pp 907–914.

[6] Levy, R., 1996, *Structural Engineering of Microwave Antennas*, IEEE Press.

[7] Greve, A., M. Dan, and J. Penalver, 1992, "Thermal Behavior of Millimeter Wavelength Radio Telescopes, *IEEE Transactions on Antenna and Propagation*," **40** (11), pp 1375-1388.

[8] Greve, A., M. Bremer, J. Peñalver, P. Raffin, and D. Morris, 2005, "Improvement of the IRAM 30-m Telescope From Temperature Measurements and Finite-Element Calculations," *IEEE Transaction on Antennas and Propagation*, **53(**2), pp. 851-860.

[9] Chen Q., 2009, "Ventilation performance prediction for buildings: A method overview and recent applications," *Building and Environment*, **44(4)**, pp. 848-858.

[10] Gao, J., F.S.g Gao, J.-N. Zhao and Jing Liu, 2007, "Calculation of Natural Ventilation in Large Enclosures," *Indoor and Built Environment*; **16**(4), pp. 292-301.

[11] Lorenzetti, D.M, 2002, "Computational aspects of nodal multizone airflow systems," *Building and Environment* **37**(11), pp. 1083 – 1090.

[12] Togari, S., Y. Arai, K. Miura, 1993, "A simplified model for predicting vertical, temperature distribution in a large space," *ASHRAE Transactions,* **99**(1), pp. 84–99.

[13] Lin, Y., R. Zmeureanu, 2008, "Computer model of the airflow and thermal phenomena inside a large dome," *Energy and Buildings,* **40**(7), pp. 1287–1296.

[14] Ganguly, A., S. Ghosh, 2009, "Model development and experimental validation of a floriculture greenhouse under natural ventilation," *Energy and Buildings* **41** (5), pp. 521–527.

[15] ASHRAE, 1987, ASHRAE Handbook - HVAC Systems and Applications, *American Society of Heating, Refrigeration and Air Conditioning Engineers*.

[16] Incropera, F., and D. DeWitt, 1996, *Introduction to Heat Transfer*, John Wiley & Sons, Inc..

[17] Kays, W.M., and M. E. Crawford, 1980, *Convective Heat and Mass Transfer*, 2nd edition, McGraw-Hill.

[18] ESSCO, 1989, Interior Climate Controls for Radomes, Internal Report.

8 APPENDIX A: FOURIER SERIES CONSTANTS

The Fourier series constants for equation 5 are given as follows:

	T_{∞_o}
February	2.74E+02
April	2.83E+02
August	2.96E+02
October	2.84E+02

T_{∞_An}				
n	February	April	August	October
1	1.04E+00	1.37E+00	1.69E+00	1.32E+00
2	-9.20E-01	-1.20E+00	-9.67E-01	-1.03E+00
3	2.88E-01	1.67E-01	-7.40E-02	1.66E-01
4	-1.98E-01	-1.53E-01	-3.06E-01	-3.70E-01
5	-1.01E-02	-1.57E-02	-1.96E-01	-4.40E-02
6	-5.96E-02	-1.94E-01	-7.93E-02	-9.84E-02
T_{∞_Bn}				
n	February	April	August	October
1	-1.80E+00	-3.93E+00	-5.04E+00	-3.79E+00
2	5.66E-03	3.56E-01	-8.40E-02	3.13E-01
3	7.10E-02	-3.18E-02	-6.56E-01	-2.57E-01
4	-4.20E-02	2.01E-01	1.84E-01	1.14E-01
5	1.77E-01	-4.62E-02	-1.95E-01	1.60E-01
6	1.36E-01	1.94E-01	2.06E-01	2.97E-01

	Q_{solar_o}
February	2.86E+02
April	3.16E+02
August	3.09E+02
October	2.76E+02

Q_{solar_An}				
n	February	April	August	October
1	-2.36E+02	-2.49E+02	-2.43E+02	-2.30E+02
2	-1.24E+02	-1.08E+02	-1.04E+02	-1.24E+02
3	4.33E+01	7.39E+00	5.86E+00	5.09E+01
4	2.17E+01	1.88E+01	1.81E+01	1.97E+01
5	1.43E+01	1.01E+00	6.32E-01	1.55E+01
6	9.71E+00	1.42E+01	1.39E+01	6.30E+00
Q_{solar_Bn}				
n	February	April	August	October
1	-4.09E+02	-4.31E+02	-4.20E+02	-3.98E+02
2	2.14E+02	1.86E+02	1.80E+02	2.15E+02
3	1.43E-13	1.45E-13	1.34E-13	1.40E-13
4	3.75E+01	3.25E+01	3.14E+01	3.41E+01
5	-2.48E+01	-1.74E+00	-1.09E+00	-2.69E+01
6	2.81E-13	2.91E-13	2.89E-13	2.83E-13